JOURNAL OF THERMOPHYSICS AND HEAT TRANSFER
Vol. 23, No. 1, January–March 2009

Development and Verification of a One-Dimensional Ablation Code Including Pyrolysis Gas Flow

A. J. Amar*
Sandia National Laboratories, Albuquerque, New Mexico 87185-0825
and North Carolina State University, Raleigh, North Carolina 27695-7910
B. F. Blackwell†
Blackwell Consulting, Corrales, New Mexico 87048
and
J. R. Edwards‡
North Carolina State University, Raleigh, North Carolina 27695-7910

DOI: 10.2514/1.36882

The development and verification of a one-dimensional material thermal response code with ablation is presented. The implicit time integrator, control volume finite element spatial discretization, and Newton's method for nonlinear iteration on the entire system of residual equations have been implemented and verified for the thermochemical ablation of internally decomposing materials. The study covers decomposing materials including decomposition kinetics, pyrolysis gas flow through the porous char layer, and a mixture (solid and gas) energy equation. A verification problem intended to examine the implementation of the math model is presented for the thermochemical ablation of a carbon–phenolic ablator that exercises every term in the system of governing equations.

Nomenclature

A	=	area
$\mathbf{A}$	=	area vector
C_v	=	specific heat at constant volume
E	=	activation energy in Arrhenius relationship
$\dot{E}$	=	energy transfer rate due to control volume convection
$\tilde{E}$	=	energy content
e	=	specific internal energy
(e)	=	element
$\dot{G}$	=	energy transfer rate from gas flux
h	=	specific enthalpy
h_f^o	=	heat of formation
k	=	thermal conductivity or preexponential factor in Arrhenius relationship
L	=	time-dependent domain length
$\hat{M}$	=	molecular weight
$\check{M}$	=	gas mass flux with grid convection contribution
$\tilde{M}$	=	gas mass content
$\dot{m}''$	=	mass flux
$\dot{m}'''$	=	volumetric mass source term
$\mathbf{Q}$	=	volumetric flow rate vector
$\dot{Q}$	=	heat conduction rate
$\dot{q}''$	=	heat flux
$\dot{\mathbf{q}}''$	=	heat flux vector
$\mathbf{R}$	=	residual vector
$\hat{R}$	=	universal gas constant
s	=	surface recession
$\dot{s}$	=	surface recession rate
T	=	temperature
t	=	time
u	=	velocity
u'	=	superficial velocity
V	=	volume
$\mathbf{v}$	=	velocity vector
$\mathbf{v}'$	=	superficial velocity vector
w	=	dimensionless relative density
x	=	coordinate with respect to instantaneous ablation front
y	=	mass fraction
z	=	coordinate with respect to initial ablation front
α	=	thermal diffusivity
β	=	extent of reaction (degree of char)
Γ	=	initial resin volume fraction
ϵ	=	emissivity
η	=	Landau coordinate
Θ	=	time rate of change of temperature
κ	=	permeability
μ	=	dynamic viscosity
ρ	=	density
ϕ	=	porosity
ψ	=	reaction order in Arrhenius relationship

Subscripts

A, B, C	=	solid composite components
c	=	char
cs	=	control surface
cv	=	control volume
g	=	gas
i	=	composite component index
j	=	nodal or element indices
o	=	initial value
s	=	solid
v	=	virgin plastic

Superscripts

converged	=	converged value
g.c.	=	globally converged value

Presented as Paper 4535 at the 39th AIAA Thermophysics Conference, Miami, FL, 25–28 June 2007; received 28 January 2008; revision received 9 August 2008; accepted for publication 11 August 2008.

*Currently employed by NASA Johnson Space Center, Houston, Texas, 77058. Member AIAA.
†Consultant. Associate Fellow AIAA.
‡Associate Professor, Department of Mechanical and Aerospace Engineering. Associate Fellow AIAA.

n = time level
ν = iteration level

I. Introduction

NUMERICAL heat transfer and ablation modeling have been important tools in the design and analysis of rocket nozzles and reentry vehicle heat shields because they provide a means of simulating material thermal response including transient heat conduction, shape change, and in-depth decomposition. Improved accuracy in the predictions of mass loss and energy transfer related to thermal protection systems helps reduce vehicle performance uncertainty and design margin, which could lead to a reduction in vehicle weight.

In the 1960s, Moyer and Rindal [1] developed a one-dimensional, finite difference ablation code (charring materials ablation, or CMA) that employed a translating grid scheme in which the grid was attached to the receding surface and the overall number of nodes in the domain would be reduced as mass was removed at the ablating surface. Moyer and Rindal used a fully implicit time integrator and lagged the temperature dependent material properties and surface recession rate at the interior nodes while the nonlinear surface energy balance was solved iteratively to give the updated surface recession rate and surface temperature. Explicit integration of the solid energy equation has also been attempted by Moyer and Rindal during the development of CMA and, more recently, in a finite volume code by Suzuki et al. [2]. In 1988, Blackwell [3] presented the control volume finite element method (CVFEM) for solving ablation problems on translating/node-dropping grids with a fully implicit time integrator with which he implemented the Moyer and Rindal approach to iterating only on the nonlinear surface energy balance.

Later, a contracting grid scheme for one-dimensional ablation was presented by Blackwell and Hogan [4], in which the relative size of the grid cells and the total number of cells remains fixed throughout the problem, and each node translates at a fraction of the surface recession rate. This eliminates the node-dropping complexity, but adds a change in energy storage due to cell volume reduction. This method also has a more logical extension to multidimensional space as presented by Hogan et al. [5]. Blackwell's and Hogan's works also implemented the CVFEM with a fully implicit time integrator that again iterated only on the surface energy balance to determine recession rate. More recent studies on one-dimensional and multidimensional ablation modeling and application work can be attributed to Suzuki et al. [6,7] and Chen and Milos [8–11] and Chen et al. [12].

The current study is a presentation of the development and verification of a one-dimensional thermal response and ablation code using the CVFEM, a contracting grid scheme, and fully implicit time integration. Although the model has been developed for planar, cylindrical, and spherical geometries with fully implicit and trapezoidal time integrators, only the process for planar geometries with the implicit time integrator is presented here. This is a simplification to show the development, verification, and usability of the method. The development and verification of the conduction, capacitance, and grid convection terms as well as the ablation boundary conditions associated with nondecomposing ablators has been presented previously by the authors [13]. The current work concentrates on the verification of the in-depth decomposition (pyrolysis) and porous flow models. The governing equations are solved using the Gauss–Seidel segregated solution procedure with Newton subiteration for the gas continuity and mixture energy equations. Newton's method with analytical sensitivities is used to iterate on the entire system of nodal residual equations to determine the time-accurate temperature and density dependent material properties and surface recession rate. Newton's method is used to solve the segregated mixture energy and gas phase continuity equations whereas direct integration of the decomposition kinetics is used to update the solid density.

The differences or improvements in the current study when compared with legacy codes include the addition of the gas phase continuity equation with porous flow, the block Gauss–Seidel method combined with Newton iteration on the entire system of residual equations using analytical Jacobian terms to determine time-accurate nonlinearities, improved decomposition kinetics, and, most importantly, the verification of the proper implementation of the model.

Modern software development should include both formal verification and validation studies to ensure that the model equations have been implemented correctly and that they properly account for the physics of the problem being solved. It is the intent of the authors to show the algorithm development and systematic verification process that was adopted throughout this code development project because verification results for similar codes are sparse. As a result, the physical model presented in this work does not apply to any specific ablation problem that an analyst or researcher may be faced with, but the software development approach and novel solution procedure for this class of problems can be extended to include more complicated and applicable physics. The results presented in this paper are a necessary step in the process of developing an ablation code with more complex physical models. Code developers often have the tendency to skip directly to "validating" their codes by comparing them with legacy codes and available experimental data. However, it should be noted that the first step in the formal validation process is to verify the implementation of the model [14]. Again, code verification is what is highlighted in this work and no attempt is made to validate the physical model by comparing it with experimental data, although a solution to a real-world problem is presented.

For brevity's sake, many of the sensitivity derivations are excluded from this document, but complete derivation, implementation, and verification details are presented by Amar [15].

II. Governing Equations

The equations that govern the solid/gas system of the porous charring ablator include solid energy and continuity equations as well as the Navier–Stokes equations as applied to all the gaseous species considered. In general, it is possible that the pyrolysis gases react among themselves, erode the remaining solid, or deposit residue (coke) on the solid, but these phenomena are neglected. Under the assumptions that the pyrolysis gas is a single nonreactive entity, the kinetic energy of the gas can be neglected, the solid and gas are in thermal equilibrium, and there is no in-depth energy source, then the solid and gas energy equations for a moving grid reduce to a mixture energy equation given by

$$\underbrace{\int_{\text{cs}} \dot{\mathbf{q}}'' \cdot \mathrm{d}\mathbf{A}}_{\text{conduction}} + \underbrace{\int_{\text{cs}} \phi \rho_g h_g \mathbf{v}_g \cdot \mathrm{d}\mathbf{A}}_{\text{gas flux}} - \underbrace{\int_{\text{cs}} \rho h \mathbf{v}_{\text{cs}} \cdot \mathrm{d}\mathbf{A}}_{\text{grid convection}} + \frac{\mathrm{d}}{\mathrm{d}t} \underbrace{\int_{\text{cv}} \rho e \cdot \mathrm{d}V}_{\text{energy content}} = 0 \tag{1}$$

and the mixture continuity equation given by

$$\underbrace{\int_{\text{cs}} \phi \rho_g \mathbf{v}_g \cdot \mathrm{d}\mathbf{A}}_{\text{gas flux}} - \underbrace{\int_{\text{cs}} \rho \mathbf{v}_{\text{cs}} \cdot \mathrm{d}\mathbf{A}}_{\text{grid convection}} + \frac{\mathrm{d}}{\mathrm{d}t} \underbrace{\int_{\text{cv}} \rho \mathrm{d}V}_{\text{mass content}} = 0 \tag{2}$$

which is the sum of the solid phase continuity equation:

$$\frac{\mathrm{d}}{\mathrm{d}t} \underbrace{\int_{\text{cv}} \rho_s \, \mathrm{d}V}_{\text{solid mass content}} - \underbrace{\int_{\text{cs}} \rho_s \mathbf{v}_{\text{cs}} \cdot \mathrm{d}\mathbf{A}}_{\text{grid convection}} = \underbrace{\int_{\text{cv}} \dot{m}_s''' \, \mathrm{d}V}_{\text{solid mass source}} \tag{3}$$

and the gas phase continuity equation:

$$\frac{\mathrm{d}}{\mathrm{d}t} \underbrace{\int_{\text{cv}} \phi \rho_g \, \mathrm{d}V}_{\text{gas mass content}} + \underbrace{\int_{\text{cs}} \phi \rho_g \mathbf{v}_g \cdot \mathrm{d}\mathbf{A}}_{\text{gas flux}} - \underbrace{\int_{\text{cs}} \phi \rho_g \mathbf{v}_{\text{cs}} \cdot \mathrm{d}\mathbf{A}}_{\text{grid convection}} = \underbrace{\int_{\text{cv}} \dot{m}_g''' \, \mathrm{d}V}_{\text{gas mass source}} \tag{4}$$

where

$$\int_{cv} \dot{m}_g''' \, dV + \int_{cv} \dot{m}_s''' \, dV = 0 \tag{5}$$

Applying the Navier–Stokes momentum equations to flow through the char layer would require detailed knowledge of the pore structure, and that information is not known. Instead, Darcy's law [16] is used, and it relates the volumetric flow rate ($\boldsymbol{Q}$) of a laminar flowing fluid to the local pressure gradient within a fully saturated porous medium by

$$\boldsymbol{Q} = -A\frac{\kappa}{\mu}\nabla P \tag{6}$$

The superficial or filtration velocity is the volumetric flow rate averaged over the cross-sectional area of the medium and is given by

$$\mathbf{v}' = \frac{\boldsymbol{Q}}{A} = -\frac{\kappa}{\mu}\nabla P \tag{7}$$

It should be noted that this method can easily be applied to other porous flow models, but Darcy's law was used as a first attempt and will be presented here. The validity of any porous flow model relies heavily on whether or not a given problem falls within the range of applicability of the model, which is low Reynolds number porous flows for Darcy's law. Also, the accuracy of any model will be greatly affected by the fidelity of the material properties that are supplied to it, but accurate material properties are not required to verify model implementation. The model presented here has been recently extended by Martin and Boyd [17] to include additional terms in the porous flow law to extend the applicability to other flow regimes.

Because the momentum equation for the pyrolysis gases is assumed to be Darcy's law, which provides a simple relationship between the fluid velocity and the pressure gradient, Darcy's law in conjunction with the perfect gas law is treated as a closure relationship for the energy-continuity system of equations with the following dependent variables: surface recession rate, temperature, solid density, and gas density. As a result, there is no independent solution of a momentum equation because this is inherent in the gas phase continuity equation solution.

The block Gauss–Seidel procedure uses Newton's method for a system of nonlinear equations to solve the segregated mixture energy and gas phase continuity equations. Consequently, a residual formulation, or Δ formulation, of the control volume energy and gas mass balance equations is solved, resulting in the linear system's Jacobian matrix, $[A]$ in Eq. (8), being composed of the residuals' sensitivities to the dependent variables:

$$[A]\Delta\mathbf{x} = -\mathbf{R} \tag{8}$$

As a result, convergence can be monitored as the correction vector, $\Delta\mathbf{x}$, or the residual vector, $\mathbf{R}$, approaches zero. The solid continuity equation is not solved in this manner and is instead solved through direct integration of the decomposition kinetics.

The solution procedure for the entire system of governing equations can be outlined as follows:

1) Iteratively solve the mixture energy equation with nodal temperatures and surface recession rate as the dependent variables.
   a) Adjust the grid throughout iteration procedure (the contracting grid scheme implementation is described by Amar et al. [13] and Amar [15]).
   b) Hold the nodal density and gas velocity values constant.
2) Integrate kinetic relationships to solve the solid phase continuity equation.
   a) Use the updated grid and temperature field.
3) Iteratively solve the gas phase continuity equation with nodal gas densities as the dependent variables.
   a) Use Darcy's law to determine the pyrolysis gas velocity in the pore space.
   b) Hold the solid density, temperature, and recession rate constant from the previously converged solution of the energy and solid continuity equations.

This segregated solution procedure in which updated information is being used as soon as it is available is commonly referred to as the block Gauss–Seidel method, which converges linearly if implemented correctly. Steps 1–3 are considered one global iteration and are repeated until global convergence of the Gauss–Seidel method is reached. The system is considered globally converged when no local nonlinear iteration is necessary to converge the mixture energy equation.

III. Material Model

To complete the explanation of the governing equations, it is important to understand the material model used to characterize the state of the solid/gas mixture. It is assumed that all the pores are interconnected; therefore, pyrolysis gases occupy all of the pore space and are free to flow through it. Consequently, the density of the solid/gas mixture is described by

$$\rho = \phi\rho_g + \rho_s \tag{9}$$

where the solid density is a bulk density, the gas density is a true density, and the porosity is equal to the gas volume fraction.

It is assumed that the thermodynamic state of the pyrolysis gases can be described by the perfect gas law, and that the solid and gas phases are in thermal equilibrium resulting in

$$P = \rho_g \frac{\hat{R}}{\hat{M}_g(T)} T \tag{10}$$

The solid material model adopted in this study is similar to the model used in CMA and is consistent with many of the studies mentioned in the Introduction. The solid bulk density is given by

$$\rho_s = \underbrace{\Gamma(\rho_A + \rho_B)}_{\text{resin}} + \underbrace{(1-\Gamma)\rho_C}_{\text{binder}} \tag{11}$$

where Γ is the resin volume fraction in the virgin composite. The component density terms are not truly densities, but they can be more appropriately considered component concentrations. Although using the symbol ρ to represent the concentrations is misleading, this nomenclature along with the "density" verbiage will continue to be used to be consistent with the precedent established by 50 years of published studies.

It is assumed that the solid does not change volume due to thermal expansion; therefore, the mixture volume is constant. It is important to note that the solid description in Eq. (11) is only a modeling assumption, and the solid is not truly composed of three components or species. In other words, there are no distinctly distinguishable materials A, B, and C in a general decomposable resin/binder composite. This modeling assumption comes as a result of decomposition data obtained from thermogravimetric analyses. It has been observed that phenolic resins undergo a two-stage decomposition process that can be appropriately captured by the two-resin-component model [18]. The decomposition of the binder material, which occurs in asbestos and nylon phenolics, is accounted for in this model, but materials such as silica and carbon phenolics undergo no binder decomposition. The model has been extended to include any number of decomposable constituents, but the three-component model is presented here for consistency with the legacy model.

It is assumed that all decomposed solid mass results in gas mass generation, and the general model of the decomposition process is described by

$$\text{virgin plastic} \Rightarrow \text{char} + \text{gas}$$

This is a generalized description of the initial and final states of the system between which there are transitional states at which the solid can exist. The reaction is irreversible, and the pyrolysis gases are

assumed to not react among themselves or with the remaining solid in the pore space.

Taking the temporal derivative of Eq. (11) gives the solid decomposition rate in terms of component decomposition rates:

$$\frac{\partial \rho_s}{\partial t} = \Gamma\left(\frac{\partial \rho_A}{\partial t} + \frac{\partial \rho_B}{\partial t}\right) + (1-\Gamma)\frac{\partial \rho_C}{\partial t} \tag{12}$$

It is assumed that the decomposition of each component can be described by an Arrhenius relationship of the form

$$\frac{\partial \rho_i}{\partial t} = -k_i \rho_{v_i}\left(\frac{\rho_i - \rho_{c_i}}{\rho_{v_i}}\right)^{\psi_i} e^{-E_i/RT} \quad \text{for } i = A, B, \text{ and } C \tag{13}$$

which applies at a constant spatial location.

Because most thermophysical properties of the solid are only known for the virgin plastic and fully charred states, the intermediate solid is modeled as some interpolated state between virgin and char. This interpolated state is characterized by the extent of reaction (β), or degree of char, given by

$$\beta = \frac{\rho_v - \rho_s}{\rho_v - \rho_c} \tag{14}$$

where the virgin and char bulk densities are known constants. It is evident that, as the solid decomposes from virgin to char, the extent of reaction ranges from 0 to 1. The definition in Eq. (14) can be rearranged to more clearly describe the interpolated state:

$$\rho_s = (1-\beta)\rho_v + \beta\rho_c \tag{15}$$

Although the virgin and char materials are not distinguishable entities within the intermediate solid, Eqs. (14) and (15) reveal that the degree of char represents an "imaginary" char volume fraction within the solid (not in the solid/gas mixture). In a similar light, Moyer and Rindal [1] defined an imaginary virgin mass fraction given by

$$y_v = \frac{\rho_v}{\rho_v - \rho_c}(1 - (\rho_c/\rho_s)) \tag{16}$$

which can be related to the extent of reaction through

$$y_v = (\rho_v/\rho_s)(1-\beta) \tag{17}$$

Similarly, the char mass fraction is given by

$$y_c = 1 - y_v = (\rho_c/\rho_s)\beta \tag{18}$$

These imaginary parameters are used to determine several solid and mixture properties.

IV. Property Models

A summary of the thermophysical and thermodynamic properties that are input parameters is given in Table 1 and a discussion of the properties required for the solution of the governing equations follows. The listed functions in Table 1 are all tabulated functions of the designated variable. Tabulated surface thermochemical data is also supplied to the code for the ablation boundary condition that is described by Amar [15].

A. Specific Internal Energy, Gas Enthalpy, and Specific Heat Models

The specific internal energy of the mixture will take into account both the solid and gas phases. The solid specific internal energy and enthalpy can be found from

$$e_s(T) = h_s(T) = y_v e_v(T) + (1-y_v)e_c(T) \tag{19}$$

Because the code is supplied with piecewise linear specific heat functions in the form of tables, $e_v(T)$ and $e_c(T)$ should be determined through integration of their respective specific heat tables [15]. The gas specific internal energy can be found from

$$e_g(T) = h_g(T) - (P/\rho_g) \tag{20}$$

Table 1 Thermophysical and thermodynamic property input parameters

Input parameter	Description
$C_{v_v}(T)$	Specific heat of the virgin material
$C_{v_c}(T)$	Specific heat of the char material
T_{ref}	Reference temperature for heats of formation
$(h_f^o)_v$	Virgin plastic heat of formation
$(h_f^o)_c$	Char heat of formation
$(h_f^o)_g$	Pyrolysis gas heat of formation
$k_v(T)$	Thermal conductivity of the virgin material
$k_c(T)$	Thermal conductivity of the char material
$\epsilon_v(T)$	Emissivity of the virgin material
$\epsilon_c(T)$	Emissivity of the char material
$h_g(T)$	Pyrolysis gas enthalpy
$M_g(T)$	Pyrolysis gas molecular weight
$\phi(\beta)$	Porosity
$\kappa(\beta)$	Permeability
$\mu(T)$	Pyrolysis gas dynamic viscosity

Consequently, the mixture specific internal energy and enthalpy can then be determined from

$$e(T) = y_g e_g(T) + (1-y_g)e_s(T) \tag{21}$$

and

$$h(T) = y_g h_g(T) + (1-y_g)h_s(T) \tag{22}$$

where the gas mass fraction is defined as

$$y_g = (\phi\rho_g/\rho) \tag{23}$$

The specific heats can be found in a similar manner and details are provided by Amar [15].

B. Thermal Conductivity and Emissivity

It is assumed that the virgin and char thermal conductivities and emissivities are bulk properties of the porous solid, which is a reasonable assumption because realistic experiments to determine these properties would be performed on a porous sample. In addition, it is assumed that the conductivity of the gas can be neglected; therefore, the mixture property is equal to the solid property. Unlike internal energy and specific heat, the definitions of thermal conductivity and emissivity do not inherently suggest a natural weighting parameter (volume or mass fraction). Both extent of reaction[§] and mass fraction [1] have been used in previous studies; a mass fraction weighting is used in this model. The resulting thermal conductivity and emissivity expressions are

$$k(T) = y_v k_v(T) + (1-y_v)k_c(T) \tag{24}$$

and

$$\epsilon(T) = y_v \epsilon_v(T) + (1-y_v)\epsilon_c(T) \tag{25}$$

It is necessary to note that determining thermal conductivity and emissivity using mass weighted averages of the virgin and char states is strictly a modelling assumption to apply a physically meaningful property to the intermediate solid. There are no experimental data to ensure that these assumptions are correct, but available data are limited to virgin and char properties and so an appropriate assumption must be made.

C. Porosity, Permeability, Viscosity, and Molecular Weight

The solution to the governing equations also accounts for variable porosity, permeability, pyrolysis gas viscosity, and pyrolysis gas molecular weight, and these properties are determined by linear

[§]Hickox, C. E., "Numerical Simulation of the Thermally-Induced Decomposition of a Porous Material," Sandia National Laboratories internal memorandum, Albuquerque, NM, 1997.

interpolation in the tabulated functions described in Table 1. Because the porosity and permeability data are known for the intermediate solid and both quantities are assumed to have no dependence on temperature, they are tabulated as functions of extent of reaction and, beyond interpolation, no further calculations are necessary to determine these properties.

V. Mixture Energy Equation

The mixture energy conservation equation is given in Eq. (1), and the discretization of each term is discussed in the subsequent sections. For both the mixture energy and gas mass conservation equations, a consistent sign convention is adopted such that

$$[\text{outflow terms}] - [\text{inflow terms}] + [\text{rate of change of content}] = [\text{source terms}]$$

For one dimension, Eq. (1) in semidiscrete form for a nodal control volume becomes

$$\begin{aligned} 0 = {} & (\dot{q}''A)_{j+1/2} - (\dot{q}''A)_{j-1/2} - (\phi\rho_g h_g u_g A)_{j-1/2} \\ & + (\phi\rho_g h_g u_g A)_{j+1/2} + (\rho h u_{cs} A)_{j-1/2} - (\rho h u_{cs} A)_{j+1/2} \\ & + \frac{d}{dt}\int_{\bar{z}_{j-1}}^{z_j} \rho e A \mathrm{d}z + \frac{d}{dt}\int_{z_j}^{\bar{z}_j} \rho e A \mathrm{d}z \end{aligned} \tag{26}$$

where the energy balance terms can be seen in Fig. 1. Section IV presented the model for determining thermophysical and thermodynamic properties of the gas, solid, and mixture that are necessary for the solution of the mixture energy equation.

When solving the mixture energy equation, nodal temperatures and the surface recession rate are treated as the dependent variables whereas nodal values of solid density, gas density, and gas velocity are constant. The nodal gas velocity is held constant because the flow work associated with the moving gas is small compared with the internal energy of the solid. Therefore, recalculating the gas velocity and its associated sensitivities during every energy equation iteration would not be expected to accelerate global convergence or reduce computational time.

For nonablating intervals (when the surface recession rate is zero), the linear system in Eq. (8) is tridiagonal because the only unknowns in the residual equations are nodal temperature corrections. The linear system for a five node domain is given by

$$\begin{bmatrix} b_1 & c_1 & 0 & 0 & 0 \\ a_2 & b_2 & c_2 & 0 & 0 \\ 0 & a_3 & b_3 & c_3 & 0 \\ 0 & 0 & a_4 & b_4 & c_4 \\ 0 & 0 & 0 & a_5 & b_5 \end{bmatrix}^{\nu} \begin{bmatrix} \Delta T_1 \\ \Delta T_2 \\ \Delta T_3 \\ \Delta T_4 \\ \Delta T_5 \end{bmatrix}^{\nu+1} = \begin{bmatrix} d_1 \\ d_2 \\ d_3 \\ d_4 \\ d_5 \end{bmatrix}^{\nu} \tag{27}$$

On the other hand, when the material is ablating, the residual equations have a nonlinear dependence on the surface recession rate.

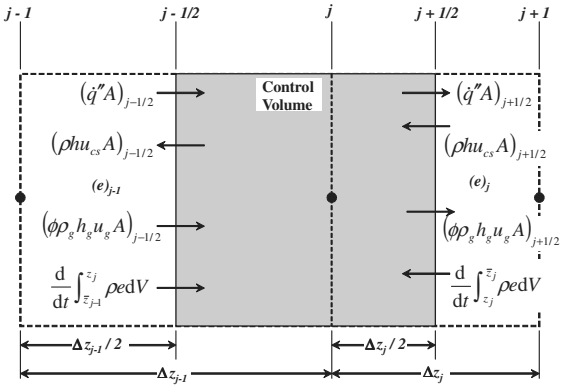

Fig. 1 Energy balance terms for the control volume surrounding node *j*.

The resulting linear system, for the same five node domain, is of the form

$$\begin{bmatrix} e_0 & c_0 & 0 & 0 & 0 & 0 \\ e_1 & b_1 & c_1 & 0 & 0 & 0 \\ e_2 & a_2 & b_2 & c_2 & 0 & 0 \\ e_3 & 0 & a_3 & b_3 & c_3 & 0 \\ e_4 & 0 & 0 & a_4 & b_4 & c_4 \\ e_5 & 0 & 0 & 0 & a_5 & b_5 \end{bmatrix}^{\nu} \begin{bmatrix} \Delta\dot{s} \\ \Delta T_1 \\ \Delta T_2 \\ \Delta T_3 \\ \Delta T_4 \\ \Delta T_5 \end{bmatrix}^{\nu+1} = \begin{bmatrix} d_0 \\ d_1 \\ d_2 \\ d_3 \\ d_4 \\ d_5 \end{bmatrix}^{\nu} \tag{28}$$

where the vector **e** in the first column of the sensitivity matrix contains residuals' sensitivities to the surface recession rate. It is evident that an additional relationship to provide the "zeroth" residual equation is necessary for the solution of this system, and this relationship is provided by the ablation model. The discussion of the ablation models and other boundary conditions for both the mixture energy and gas phase continuity equations is omitted from this paper for brevity's sake, but a detailed discussion is given by Amar [15].

For simulations that have both ablating and nonablating intervals, the code switches between a tridiagonal solver and a linear system solver tailored for the system in Eq. (28) to minimize computational time. Timing study results presented by Amar et al. [13,15] show that, given the same convergence criteria, solving a problem with the entire recession rate sensitivity vector is more computationally efficient than solving the problem with the purely tridiagonal formulation traditionally used in legacy codes.

An element assembly approach to generating the global sensitivity matrix entries is used for the mixture energy and gas phase continuity equations. As a result, each term in the governing equations is discretized on an element-by-element basis and the appropriate contributions are made to the nodal control volume residual equations. Consequently, each element, $(e)_j$, has contributions to the residual equations associated with nodes j and $j+1$, as seen in Fig. 1.

A. Conduction

Fourier's law is used to model the heat conducted at a control volume boundary, and the heat conduction rate is given by

$$\dot{Q}_{j+1/2} = \left[-k(T)A\frac{\mathrm{d}T}{\mathrm{d}z}\right]_{j+1/2} = \frac{-\bar{k}(T)A}{\Delta z_j}(T_{j+1} - T_j) \tag{29}$$

where $\bar{X} = X_{j+1/2} = X_{\bar{z}_j} = (X_{j+1} + X_j)/2$ and X is any quantity. The elemental representation of the heat conduction rate is

$$\begin{bmatrix} \dot{Q}_j \\ \dot{Q}_{j+1} \end{bmatrix} = \frac{\bar{k}(T)A}{\Delta z_j}\begin{bmatrix} 1 & -1 \\ -1 & 1 \end{bmatrix}\begin{bmatrix} T_j \\ T_{j+1} \end{bmatrix} \tag{30}$$

In general, the heat conduction vector is a nonlinear function of temperature and recession rate because the thermal conductivity depends on temperature and Δz_j depends on the surface recession rate. Therefore an iterative solution procedure is necessary to solve for the time-accurate nonlinearities. To aid in the iterative process, it is convenient to linearize the element conduction vector with a Taylor series expansion in iteration space treating the nodal temperatures and surface recession rate as the independent variables:

$$\begin{aligned} \begin{bmatrix} \dot{Q}_j \\ \dot{Q}_{j+1} \end{bmatrix}^{\nu+1} = {} & \begin{bmatrix} \dot{Q}_j \\ \dot{Q}_{j+1} \end{bmatrix}^{\nu} \\ & + \begin{bmatrix} \frac{\partial\dot{Q}_j}{\partial\dot{s}} & \frac{\partial\dot{Q}_j}{\partial T_j} & \frac{\partial\dot{Q}_j}{\partial T_{j+1}} \\ \frac{\partial\dot{Q}_{j+1}}{\partial\dot{s}} & \frac{\partial\dot{Q}_{j+1}}{\partial T_j} & \frac{\partial\dot{Q}_{j+1}}{\partial T_{j+1}} \end{bmatrix}\begin{bmatrix} \Delta\dot{s} \\ \Delta T_j \\ \Delta T_{j+1} \end{bmatrix}^{\nu+1} + \cdots \end{aligned} \tag{31}$$

Performing the required differentiation for planar geometry ($A(z) = 1$) gives

$$\left.\begin{aligned}
\frac{\partial \dot{Q}_j}{\partial \dot{s}} &= -\frac{\bar{k}A}{\Delta z_j^2}(T_j - T_{j+1})\frac{\partial \Delta z_j}{\partial \dot{s}} \\
\frac{\partial \dot{Q}_{j+1}}{\partial \dot{s}} &= \frac{\bar{k}A}{\Delta z_j^2}(T_j - T_{j+1})\frac{\partial \Delta z_j}{\partial \dot{s}} \\
\frac{\partial \dot{Q}_j}{\partial T_j} &= \frac{\bar{k}A}{\Delta z_j}\left[1 + \frac{(T_j - T_{j+1})}{2\bar{k}}\left(\frac{\partial k}{\partial T}\right)_j\right] \\
\frac{\partial \dot{Q}_j}{\partial T_{j+1}} &= \frac{\bar{k}A}{\Delta z_j}\left[-1 + \frac{(T_j - T_{j+1})}{2\bar{k}}\left(\frac{\partial k}{\partial T}\right)_{j+1}\right] \\
\frac{\partial \dot{Q}_{j+1}}{\partial T_j} &= \frac{\bar{k}A}{\Delta z_j}\left[-1 - \frac{(T_j - T_{j+1})}{2\bar{k}}\left(\frac{\partial k}{\partial T}\right)_j\right] \\
\frac{\partial \dot{Q}_{j+1}}{\partial T_{j+1}} &= \frac{\bar{k}A}{\Delta z_j}\left[1 - \frac{(T_j - T_{j+1})}{2\bar{k}}\left(\frac{\partial k}{\partial T}\right)_{j+1}\right]
\end{aligned}\right\} \tag{32}$$

where

$$\frac{\partial \Delta z_j}{\partial \dot{s}} = \Delta t^{n+1}(\eta_{j+1} - \eta_j) = \Delta t^{n+1}\Delta\eta_j \tag{33}$$

and the Landau coordinate is defined as

$$\eta = ((L - x)/L) = ((L_o - z)/(L_o - s)) \tag{34}$$

Note that, for cylindrical and spherical one-dimensional geometries, the area variation is a function of position ($A = A(z)$) resulting in additional terms in the surface recession rate sensitivities for all the terms discussed.

B. Grid Convection

The energy transfer rate due to convection of a control volume boundary is given by

$$\dot{E} = (\rho h u_{\mathrm{cs}} A)_{j+1/2} \tag{35}$$

and the corresponding element convection vector, invoking the mixture enthalpy definition from Eq. (22), is

$$\begin{bmatrix} \dot{E}_j \\ \dot{E}_{j+1} \end{bmatrix} = [(\phi\rho_g h_g)_{j+1/2} + (\rho_s h_s)_{j+1/2}](u_{\mathrm{cs}}A)_{j+1/2}\begin{bmatrix} -1 \\ 1 \end{bmatrix} \tag{36}$$

The control surface velocity according to the contracting grid scheme is given by

$$(u_{\mathrm{cs}})_{j+1/2} = \dot{s}\bar{\eta}_j \tag{37}$$

and the sensitivities can be derived in a similar fashion to the conduction term in Sec. V.A.

C. Gas Flux

For both moving and stationary grid problems, in-depth decomposition of the material may be occurring, which results in gas generation and convection within the porous material. The superficial gas velocity at control volume boundaries is determined from Darcy's law, which is given in one-dimensional discrete form at the control volume boundary as

$$u_g' = \frac{\bar{\kappa}}{\bar{\mu}}\frac{P_j - P_{j+1}}{\Delta z_j} \tag{38}$$

Because the permeability can vary several orders of magnitude between adjacent nodes for some materials, the averaging technique proposed in this study may not be the ideal approach for all situations and other methods could easily be implemented. Other averaging techniques such as harmonic mean approaches have been used for ablation problems and may be more appropriate for some materials [19].

The element energy convection vector from gas flux is given by

$$\begin{bmatrix} \dot{G}_j \\ \dot{G}_{j+1} \end{bmatrix} = u_g'(\rho_g h_g A)_{j+1/2}\begin{bmatrix} 1 \\ -1 \end{bmatrix} \tag{39}$$

and the sensitivities can be derived in a similar fashion to the conduction term in Sec. V.A.

D. Energy Content and Time Integration

The energy content for an element can be divided into terms corresponding to each of the two subcontrol volumes within an element.

$$\begin{bmatrix} \tilde{E}_j \\ \tilde{E}_{j+1} \end{bmatrix} = \begin{bmatrix} \int_{z_j}^{\bar{z}_j} \rho e(T) A\,\mathrm{d}z \\ \int_{\bar{z}_j}^{z_{j+1}} \rho e(T) A\,\mathrm{d}z \end{bmatrix} \tag{40}$$

The internal energy per unit volume in Eq. (40) can be expressed by a Taylor series expansion in position about the element center, and the resulting elemental energy content vector can be expressed as

$$\begin{bmatrix} \tilde{E}_j \\ \tilde{E}_{j+1} \end{bmatrix} = \begin{bmatrix} \int_{z_j}^{\bar{z}_j} (\overline{\rho e} + \frac{\partial(\rho e)}{\partial z}|_{z=\bar{z}_j}(z - \bar{z}_j))A\,\mathrm{d}z \\ \int_{\bar{z}_j}^{z_{j+1}} (\overline{\rho e} + \frac{\partial(\rho e)}{\partial z}|_{z=\bar{z}_j}(z - \bar{z}_j))A\,\mathrm{d}z \end{bmatrix} \tag{41}$$

which can be integrated for planar geometries ($A(z) = 1$) to give

$$\begin{bmatrix} \tilde{E}_j \\ \tilde{E}_{j+1} \end{bmatrix} = \frac{A\Delta z_j}{2}\begin{bmatrix} \frac{3}{4} & \frac{1}{4} \\ \frac{1}{4} & \frac{3}{4} \end{bmatrix}\begin{bmatrix} (\rho e)_j \\ (\rho e)_{j+1} \end{bmatrix} \tag{42}$$

The result is simply a weighted average of nodal values where the weighting factor matrix is geometry dependent. The time rate of change of energy content according to an implicit time integrator can be expressed as

$$\frac{\mathrm{d}}{\mathrm{d}t}\begin{bmatrix} \tilde{E}_j \\ \tilde{E}_{j+1} \end{bmatrix}^{n+1} = \left\{\begin{bmatrix} \tilde{E}_j \\ \tilde{E}_{j+1} \end{bmatrix}^{n+1} - \begin{bmatrix} \tilde{E}_j \\ \tilde{E}_{j+1} \end{bmatrix}^{n}\right\}\frac{1}{\Delta t^{n+1}} \tag{43}$$

and the sensitivities can be derived in a similar fashion to the conduction term in Sec. V.A.

VI. Solid Phase Continuity Equation

Because the solid density gradient in the decomposition region is known to be much larger than the temperature gradients in the domain, a finer mesh is necessary for the solution of the solid phase continuity equation than was needed to solve the energy equation. CMA and several other studies employ a submesh scheme in which there are a given number of nodelets (or subnodes) within each element on which the solid phase continuity equation is solved. Integrated effects of the nodelet solutions are applied at nodes during the solution of the mixture energy equation. This method saves a significant amount of computational time because it avoids excessive grid points during the mixture energy equation solution. The nodelet scheme has not been implemented in the current model; therefore, each governing equation is solved on the same mesh.

Implicit integration of the solid mass conservation equation through the CVFEM and nodal mass balance equations is not performed. Instead, the procedure of Moyer and Rindal [1] was adopted; they directly integrated the kinetic relationships while accounting for the moving grid. The development of the fixed grid solid continuity equation solution procedure is presented, and the moving grid effects are considered afterwards.

A. Solution Procedure

The solid phase continuity equation on a fixed grid is given by

$$\frac{\mathrm{d}}{\mathrm{d}t}\underbrace{\int_{\mathrm{cv}} \rho_s\,\mathrm{d}V}_{\text{solid mass content}} = \underbrace{\int_{\mathrm{cv}} \dot{m}_s'''\,\mathrm{d}V}_{\text{solid mass source}} \tag{44}$$

Substituting Eq. (11) into Eq. (44) and knowing that the component source terms can be volumetrically weighted like the component densities gives

$$\frac{\mathrm{d}}{\mathrm{d}t}\int_{\mathrm{cv}}[\Gamma(\rho_A+\rho_B)+(1-\Gamma)\rho_C]\,\mathrm{d}V = \int_{\mathrm{cv}}[\Gamma(\dot{m}_A'''+\dot{m}_B''')+(1-\Gamma)\dot{m}_C'''\,\mathrm{d}V \tag{45}$$

Because the decomposition of each component is independent of the other components when coupling effects from the other governing equations are ignored, the solid phase continuity equation can be further reduced to component continuity equations given by

$$\frac{\mathrm{d}}{\mathrm{d}t}\int_{\mathrm{cv}}\rho_i\,\mathrm{d}V = \int_{\mathrm{cv}}\dot{m}_i'''\,\mathrm{d}V \quad \text{for } i=A,B, \text{ and } C \tag{46}$$

Now there are four equations [Eqs. (45) and (46)] with four unknowns (ρ_A, ρ_B, ρ_C, and ρ_s), and the procedure is to solve the component continuity equations and then determine the solid density as a postprocessing step via Eq. (11). Given the Arrhenius form in Eq. (13), the finite differential equation analogous to Eq. (46) is

$$\left.\frac{\partial\rho_i}{\partial t}\right|_z = \dot{m}_i''' = -k_i\rho_{v_i}\left(\frac{\rho_i-\rho_{c_i}}{\rho_{v_i}}\right)^{\psi_i}e^{-E_i/RT} \quad \text{for } i=A,B, \text{ and } C \tag{47}$$

Because the density history at a given location only depends on the temperature history at that location, Eq. (47) can be integrated on a location-by-location basis (accounting for the moving grid) and the updated solid density can be determined.

B. Integration of Kinetic Equations

Because ρ_{v_i} and ρ_{c_i} are constants, the kinetic equation in Eq. (47) can be rearranged to give

$$\left.\frac{\mathrm{d}w_i}{\mathrm{d}t}\right|_z = -k_i w_i^{\psi_i}e^{-E_i/RT} \quad \text{for } i=A,B, \text{ and } C \tag{48}$$

where the dimensionless relative density is given by

$$w_i = ((\rho_i-\rho_{c_i})/\rho_{v_i}) \tag{49}$$

Direct integration of Eq. (48) over one time step while treating temperature explicitly in time gives

$$w_i(z_j^{n+1},t^{n+1}) = \{[w_i(z_j^{n+1},t^n)]^{(1-\psi_i)} - \Delta t^{n+1}(1-\psi_i)k_i e^{-E_i/RT(z_j^{n+1},t^n)}\}^{\frac{1}{1-\psi_i}} \quad \text{for } \psi_i\neq 1 \tag{50}$$

and

$$w_i(z_j^{n+1},t^{n+1}) = [w_i(z_j^{n+1},t^n)]e^{-k_i\Delta t^{n+1}e^{-E_i/RT(z_j^{n+1},t^n)}} \quad \text{for } \psi_i = 1 \tag{51}$$

Equations (50) and (51) were implemented in CMA [1] to integrate the kinetic equations regardless of the temperature change over the time interval. They are applied in the current model only if the temperature at a fixed location remains constant over the time interval.

An alternative approach to determining the dimensionless relative densities at time level $n+1$ is to assume that the temperature rise rate over the time interval Δt^{n+1} is a constant, Θ.

$$\left.\frac{\mathrm{d}T}{\mathrm{d}t}\right|_z = \Theta = \frac{T(z_j^{n+1},t^{n+1})-T(z_j^{n+1},t^n)}{\Delta t} \tag{52}$$

This is consistent with the implicit time integrator's ability to, at best, capture a linear temperature rise rate because the method is first order. With this assumption, integration of Eq. (48) and solving for $w_i(z_j^{n+1},t^{n+1})$ gives

$$w_i(z_j^{n+1},t^{n+1}) = \left\{[w_i(z_j^{n+1},t^n)]^{1-\psi_i} + \frac{k_i(\psi_i-1)}{\Theta}\int_{T(z_j^{n+1},t^n)}^{T(z_j^{n+1},t^{n+1})}e^{-E_i/RT}\,\mathrm{d}T\right\}^{\frac{-1}{\psi_i-1}} \quad \text{for } \psi_i\neq 1 \tag{53}$$

and

$$w_i(z_j^{n+1},t^{n+1}) = \exp\left(\ell_n[w_i(z_j^{n+1},t^n)] - \frac{k_i}{\Theta}\int_{T(z_j^{n+1},t^n)}^{T(z_j^{n+1},t^{n+1})}e^{-E_i/RT}\,\mathrm{d}T\right) \quad \text{for } \psi_i = 1 \tag{54}$$

where the integral in Eq. (54) can be evaluated by using exponential integrals or numerical integration techniques, and Simpson's rule was chosen for this study. Because the new dimensionless relative densities are known, the component densities can be determined via Eq. (49) and the solid bulk density can now be determined.

Because problems are solved on contracting grids for which the spatial coordinate of each node changes whereas the Landau coordinate of each node is fixed, it is necessary to determine temperature and dimensionless relative density profiles at the previous time level and current nodal locations ($T(z_j^{n+1},t^n)$ and $w_i(z_j^{n+1},t^n)$). Because properties are assumed to vary linearly within elements, linear interpolation in the old (time level n) profiles is used to calculate these properties.

VII. Gas Phase Continuity Equation

The gas mass conservation equation is given in Eq. (4) and, for one dimension, its semidiscrete form for a nodal control volume is

$$0 = \frac{\mathrm{d}}{\mathrm{d}t}\int_{\bar{z}_{j-1}}^{z_j}\phi\rho_g A\,\mathrm{d}z + \frac{\mathrm{d}}{\mathrm{d}t}\int_{z_j}^{\bar{z}_j}\phi\rho_g A\,\mathrm{d}z - (\phi\rho_g u_g A)_{j-1/2} + (\phi\rho_g u_g A)_{j+1/2} + (\phi\rho_g u_{\mathrm{cs}}A)_{j-1/2} - (\phi\rho_g u_{\mathrm{cs}}A)_{j+1/2} - \int_{\bar{z}_{j-1}}^{z_j}\dot{m}_g'''A\,\mathrm{d}z - \int_{z_j}^{\bar{z}_j}\dot{m}_g'''A\,\mathrm{d}z \tag{55}$$

and the gas mass balance terms can be seen in Fig. 2.

A. Grid Convection and Gas Flux

The gas flux and grid convection terms are treated simultaneously for the gas phase continuity equation because there is not the complexity of two phases in the grid convection terms that there was in the mixture energy equation. The combined gas flux and convection terms for the $j+1/2$ boundary in element vector form are given by

$$\begin{bmatrix}\check{M}_j\\ \check{M}_{j+1}\end{bmatrix} = [\phi\rho_g A(u_g-u_{\mathrm{cs}})]_{j+1/2}\begin{bmatrix}1\\-1\end{bmatrix} \tag{56}$$

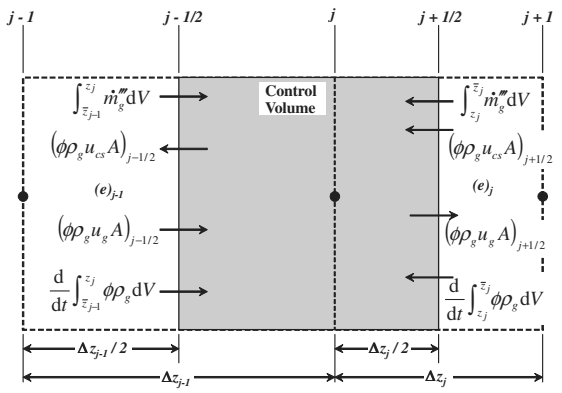

Fig. 2 Gas mass balance terms for the control volume surrounding node *j*.

Introducing the superficial velocity found from Darcy's law in Eq. (38) gives

$$\begin{bmatrix} \check{M}_j \\ \check{M}_{j+1} \end{bmatrix} = \bar{\rho}_g A[u'_g - \bar{\phi}(u_{cs})_{j+1/2}] \begin{bmatrix} 1 \\ -1 \end{bmatrix} \tag{57}$$

where

$$\phi u_g = u'_g \tag{58}$$

Linearizing the gas mass flux vector in iteration space according to a Taylor series expansion treating the nodal gas densities as the independent variables gives

$$\begin{bmatrix} \check{M}_j \\ \check{M}_{j+1} \end{bmatrix}^{v+1} = \begin{bmatrix} \check{M}_j \\ \check{M}_{j+1} \end{bmatrix}^{v} + \begin{bmatrix} \frac{\partial \check{M}_j}{\partial(\rho_g)_j} & \frac{\partial \check{M}_j}{\partial(\rho_g)_{j+1}} \\ \frac{\partial \check{M}_{j+1}}{\partial(\rho_g)_j} & \frac{\partial \check{M}_{j+1}}{\partial(\rho_g)_{j+1}} \end{bmatrix}^{v} \begin{bmatrix} \Delta(\rho_g)_j \\ \Delta(\rho_g)_{j+1} \end{bmatrix}^{v+1} + \cdots \tag{59}$$

where the sensitivity matrix entries are

$$\left.\begin{aligned} \frac{\partial \check{M}_j}{\partial(\rho_g)_j} &= A\left\{\frac{1}{2}[u'_g - \bar{\phi}(u_{cs})_{j+1/2}] + \bar{\rho}_g \frac{\partial u'_g}{\partial(\rho_g)_j}\right\} \\ \frac{\partial \check{M}_j}{\partial(\rho_g)_{j+1}} &= A\left\{\frac{1}{2}[u'_g - \bar{\phi}(u_{cs})_{j+1/2}] + \bar{\rho}_g \frac{\partial u'_g}{\partial(\rho_g)_{j+1}}\right\} \\ \frac{\partial \check{M}_{j+1}}{\partial(\rho_g)_j} &= -A\left\{\frac{1}{2}[u'_g - \bar{\phi}(u_{cs})_{j+1/2}] + \bar{\rho}_g \frac{\partial u'_g}{\partial(\rho_g)_j}\right\} \\ \frac{\partial \check{M}_{j+1}}{\partial(\rho_g)_{j+1}} &= -A\left\{\frac{1}{2}[u'_g - \bar{\phi}(u_{cs})_{j+1/2}] + \bar{\rho}_g \frac{\partial u'_g}{\partial(\rho_g)_{j+1}}\right\} \end{aligned}\right\} \tag{60}$$

Substituting the equation of state into Darcy's law gives

$$\begin{bmatrix} \frac{\partial u'_g}{\partial(\rho_g)_j} \\ \frac{\partial u'_g}{\partial(\rho_g)_{j+1}} \end{bmatrix} = \frac{\bar{\kappa}\hat{R}}{\bar{\mu}\Delta z_j} \begin{bmatrix} \left(\frac{T}{\hat{M}_g}\right)_j \\ -\left(\frac{T}{\hat{M}_g}\right)_{j+1} \end{bmatrix} \tag{61}$$

B. Gas Source

The element mass source vector is given by

$$-\begin{bmatrix} \dot{M}_j \\ \dot{M}_{j+1} \end{bmatrix} = \begin{bmatrix} -\int_{z_j}^{\bar{z}_j} \dot{m}'''_g A \, dz \\ -\int_{\bar{z}_j}^{z_{j+1}} \dot{m}'''_g A \, dz \end{bmatrix} \tag{62}$$

where the negative sign is for consistency with the established sign convention. The source term at any location can be determined by a Taylor series expansion in position about the element center, and the resulting gas mass source vector is

$$-\begin{bmatrix} \dot{M}_j \\ \dot{M}_{j+1} \end{bmatrix} = -\begin{bmatrix} \int_{z_j}^{\bar{z}_j} [\bar{\dot{m}}'''_g + \frac{\partial \dot{m}'''_g}{\partial z}|_{z=\bar{z}_j}(z - \bar{z}_j)] A \, dz \\ \int_{\bar{z}_j}^{z_{j+1}} [\bar{\dot{m}}'''_g + \frac{\partial \dot{m}'''_g}{\partial z}|_{z=\bar{z}_j}(z - \bar{z}_j)] A \, dz \end{bmatrix} \tag{63}$$

Because it is assumed that all solid decomposition results in gas generation, the nodal gas mass source terms can be determined from

$$(\dot{m}'''_g)_j^{n+1} = -(\dot{m}'''_s)_j^{n+1} = -[\Gamma(\dot{m}'''_A + \dot{m}'''_B) + (1 - \Gamma)\dot{m}'''_C]^{n+1} \tag{64}$$

Consequently, the spatial derivative of the mass source term at the element center can be determined from a central finite difference, and the gas mass source vector can be integrated for planar geometries to give

$$-\begin{bmatrix} \dot{M}_j \\ \dot{M}_{j+1} \end{bmatrix} = -\frac{\Delta z_j}{2} \begin{bmatrix} \frac{3}{4} & \frac{1}{4} \\ \frac{1}{4} & \frac{3}{4} \end{bmatrix} \begin{bmatrix} (\dot{m}'''_g)_j \\ (\dot{m}'''_g)_{j+1} \end{bmatrix} \tag{65}$$

It is evident that the mass source vector has no dependence on nodal gas density and, as a result, the mass source term has a residual vector contribution but no sensitivity matrix contributions.

C. Gas Mass Content and Time Integration

The element gas mass content vector is given by

$$\begin{bmatrix} \tilde{M}_j \\ \tilde{M}_{j+1} \end{bmatrix} = \begin{bmatrix} \int_{z_j}^{\bar{z}_j} \phi \rho_g A \, dz \\ \int_{\bar{z}_j}^{z_{j+1}} \phi \rho_g A \, dz \end{bmatrix} \tag{66}$$

A Taylor series expansion about the element center can again be used to determine the gas bulk density at any point. Integrating the resulting content vector for planar geometry gives

$$\begin{bmatrix} \tilde{M}_j \\ \tilde{M}_{j+1} \end{bmatrix} = \frac{\Delta z_j}{2} \begin{bmatrix} \frac{3}{4}\phi_j & \frac{1}{4}\phi_{j+1} \\ \frac{1}{4}\phi_j & \frac{3}{4}\phi_{j+1} \end{bmatrix} \begin{bmatrix} (\rho_g)_j \\ (\rho_g)_{j+1} \end{bmatrix} \tag{67}$$

The time rate of change of gas mass content according to an implicit time integrator can be expressed as

$$\frac{d}{dt}\begin{bmatrix} \tilde{M}_j \\ \tilde{M}_{j+1} \end{bmatrix}^{n+1} = \left\{ \begin{bmatrix} \tilde{M}_j \\ \tilde{M}_{j+1} \end{bmatrix}^{n+1} - \begin{bmatrix} \tilde{M}_j \\ \tilde{M}_{j+1} \end{bmatrix}^{n} \right\} \frac{1}{\Delta t^{n+1}} \tag{68}$$

and sensitivities can be derived in a similar fashion to the combined gas flux and convection term in Sec. VII.A.

VIII. Verification Results: Thermochemical Ablation of a Decomposing Material

A. Problem Statement

Because the correct implementation of most of the energy equation terms and boundary conditions have been previously verified (see Amar et al. [13] and Amar [15]), the decomposing material thermochemical ablation problem is intended to verify the implementation of the gas phase continuity equation in addition to the pyrolysis gas effects in the mixture energy equation. Because of the difficulty in determining an analytical solution, Richardson extrapolation [15] is used to approximate the exact solution, and the global convergence rate and nonlinear convergence rates of the mixture energy and gas phase continuity equations are determined.

Consider a 0.5-in.-thick planar slab of carbon–phenolic (with material properties given by Amar [15]) that is subject to a typical heating profile characteristic of a ballistic sphere–cone reentry body. The Stanton number is corrected for both hot wall and blowing effects, and the surface is subject to a far-field radiation condition for which the source temperature is 414.0°R and the emissivity is constant ($\epsilon = 0.85$). The back boundary is adiabatic and impermeable, and the time-dependent specified surface pressure is provided by the aerodynamic heating boundary-condition input.

B. Grid Refinement Studies

The domain was discretized with a series of four grids with $\Delta t/\Delta z_o^2 =$ constant, and the grid parameters can be seen in Table 2. More details on the motivation behind the refinement methodology are given by Amar et al. [13,15]. Because the solid continuity equation is solved by the direct integration of the decomposition kinetics, it is not obvious how its solution and, consequently, its coupling with the other governing equations will behave as the mesh is refined. As a result, an alternative procedure to the previous

Table 2 Parameters for carbon–phenolic thermochemical ablation problem grid refinement study.

Grid	No. of elem.	Δz_o, in.	Δt, s
Coarse	50	0.01	0.1
Medium	100	0.005	0.025
Fine	200	0.0025	0.00625
Extrafine	400	0.00125	0.0015625

verification problems [13,15] was used to isolate the mixture energy and gas phase continuity equations from the solid phase continuity equation solution. The procedure is as follows:

1) Solve the problem on the extrafine mesh until a problem time of $t = 25$ s is reached.
2) The conditions found at $t = 25$ s can then be used to reinitialize the problem on the entire series of grids. This results in the following: nonuniform initial profiles for all variables of interest, a contracted grid, and reinitialization while ablation is occurring.
3) Verify the mixture energy equation.
   a) Integrate over 0.1 s (restarting at $t = 25$ s) for the entire series of grids, only advancing the mixture energy equation in time while holding all other terms constant.
      i) Integration over a small time interval reduces errors associated with inconsistent nodal locations from mesh motion.
      ii) The result is as revealing as integrating over a long time interval if all the relevant terms are being employed, which is ensured by the nonuniform initialization.
   b) Perform Richardson extrapolation at $t = 25.1$ s on the surface temperature, recession rate, and back face temperature. The results showing the second-order grid convergence can be seen in Fig. 3.
4) Verify the gas phase continuity equation.
   a) Integrate over 1.0 s (restarting at $t = 25$ s) for the entire series of grids, only advancing the gas phase continuity equation in time while holding all other terms constant.
   b) Perform Richardson extrapolation at $t = 26.0$ s on the surface gas flux, an interior gas density value at a consistent spatial location, and the back face gas density. The results showing the second-order grid convergence can be seen in Fig. 4.
      i) An interior location is chosen for Richardson extrapolation on the gas density because the surface gas density is specified through the boundary conditions. $z = 1.07 \times 10^{-2}$ in. is the position of the first interior node on the coarsest mesh, which has a collocated node on each of the finer meshes.
      ii) Integration over a longer time interval was performed because the mesh does not contract during the solution of the gas phase continuity equation. Therefore, errors associated with inconsistent nodal locations will not exist when verifying the gas continuity equation.

C. Nonlinear Convergence Studies

For the mixture energy equation, the error metric used to determine the nonlinear convergence rate is the error in recession rate and is given by

$$(\text{error})^{\nu} = (\dot{s})^{\nu} - (\dot{s})^{\text{converged}} \tag{69}$$

The error metric for the gas phase continuity equation is the relative L_2 norm of the density correction vector:

$$(\text{error})^{\nu} = (L_2)^{\nu} - (L_2)^{\text{converged}} \tag{70}$$

The convergence rates are shown in Figs. 5 and 6, and the results follow the second-order trend line.

The block Gauss–Seidel method used to solve the entire system of governing equations is expected to exhibit linear convergence. Because the solution procedure achieves coupling through iteration, information can only be used as soon as it is updated and a smooth convergence curve should not be expected. To examine the global convergence, it is necessary to view the problem in global iteration space as opposed to local (Newton) iteration space. Let the iteration index (ν) now represent the global iteration. Because the solution globally converges to the exact solution plus some discretization error, the difference between the locally converged solution at a given global iteration (X^{ν}) and the globally converged solution ($X^{\text{g.c.}}$) is used as the error metric.

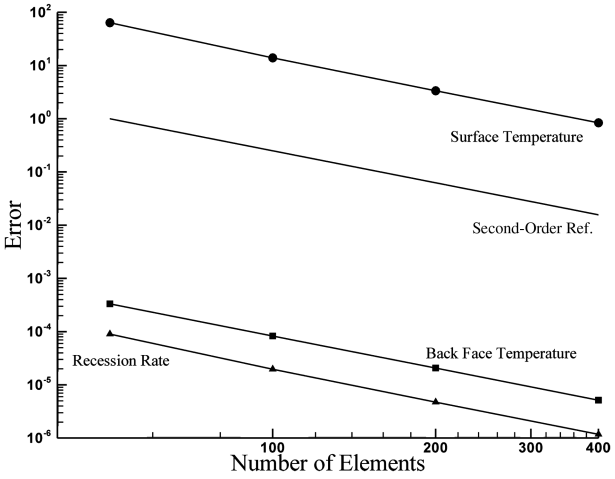

Fig. 3 Mixture energy equation grid convergence results for the carbon–phenolic thermochemical ablation verification problem.

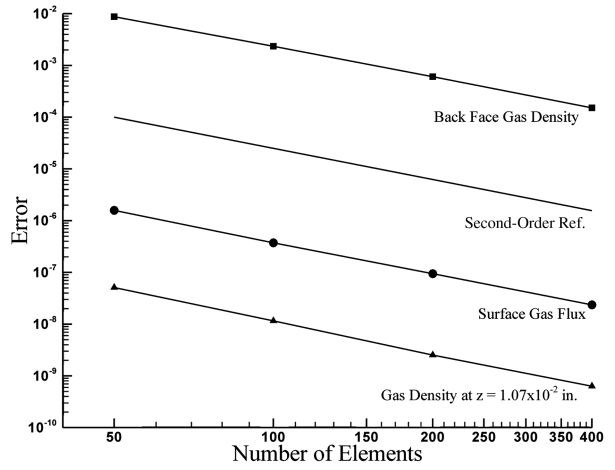

Fig. 4 Gas continuity equation grid convergence results for the carbon–phenolic thermochemical ablation verification problem.

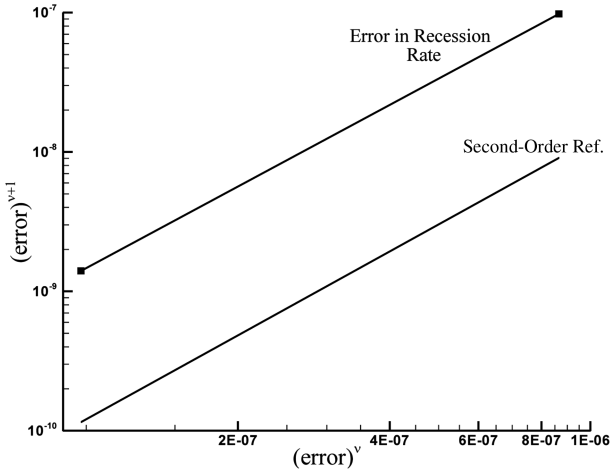

Fig. 5 Nonlinear convergence of surface recession rate for the carbon–phenolic thermochemical ablation verification problem.

$$(\text{error})^{\nu} = X^{\nu} - X^{\text{g.c.}} \tag{71}$$

The global convergence rates of the surface recession rate and gas density are shown in Fig. 7, whereas the global convergence rates for the surface temperature and solid density are shown in Fig. 8. It is

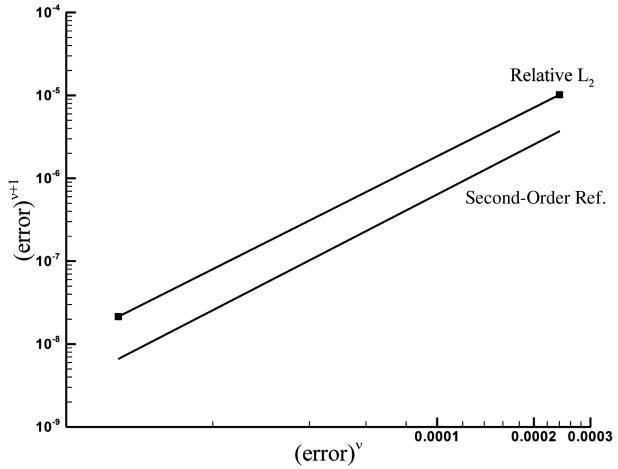

Fig. 6 Nonlinear convergence of the gas continuity equation's L_2-error norm for the carbon–phenolic thermochemical ablation verification problem.

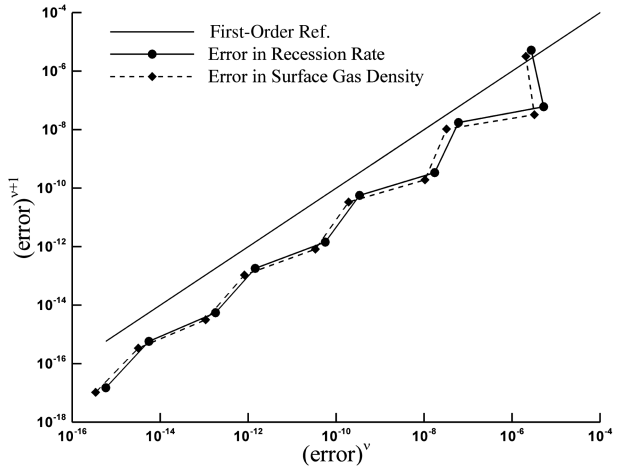

Fig. 7 Global convergence rate for the surface recession rate and gas density where ν is the global iteration index.

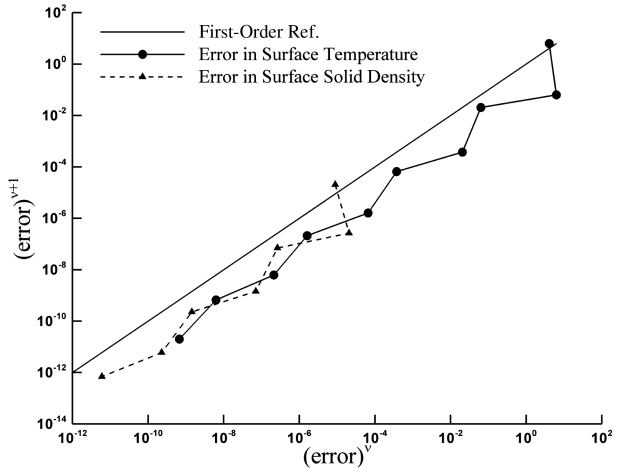

Fig. 8 Global convergence rate for the surface temperature and solid density where ν is the global iteration index.

important to note that the surface gas density only changes with surface temperature because the boundary pressure is known from the boundary conditions. As a result, the surface gas density and temperature will always converge to machine precision in the same number of global iterations. On the other hand, the surface solid density reaches global convergence in fewer iterations and experience has shown that this is generally the case.

D. Code-to-Code Comparison

Although code-to-code comparisons are not part of the formal verification process, comparisons with established codes were performed to see how the improved scheme changes the final solution. The carbon–phenolic thermochemical ablation problem was solved on the medium grid in Table 2 using both CMA and the code developed during this study. Although CMA is capable of integrating the decomposition kinetics on a finer mesh than is used to solve the mixture energy equation, this option was not exercised to make a more direct comparison. It is also important to note that the primary differences between the two codes for this simulation are as follows:

1) CMA iterates only on the surface energy balance and lags temperature-dependent properties and the surface recession rate for the interior node solution whereas the research code iterates on the entire system of residual equations to determine time-accurate nonlinearities.

2) CMA uses a translating/node-dropping grid scheme, and the research code uses a contracting grid scheme.

3) CMA uses a lumped capacitance method, and the research code uses a distributed capacitance method.

4) CMA assumes that all gas generated further in depth than a given node passes that node in the time interval in which the gas was generated and the flow work is taken into account. The research code allows internal pressure gradients to drive the flow of pyrolysis gases through the pore space.

5) CMA does not account for the gas phase internal energy in the energy capacitance term, and the research code does account for the gas phase internal energy.

6) CMA decomposition kinetics are explicit in temperature whereas the research code assumes a constant temperature rise rate over the time step.

The comparisons of the predicted surface temperature and recession rate histories can be seen in Figs. 9 and 10, respectively. Because of the number of numerical differences between the codes and the number of physical phenomena that are being modeled throughout the solution procedure, it is difficult to discern what modeling differences between the two codes are causing the discrepancy in the solutions. From these results, it is evident that CMA's pyrolysis gas assumptions, described in list items 4 and 5, are valid because including the porous flow solution (as is done in the research code) does not significantly change the mixture energy equation solution. This suggests a dominantly one-way coupling between the mixture energy equation and the gas phase continuity equation, which is expected because gas velocities are low and the

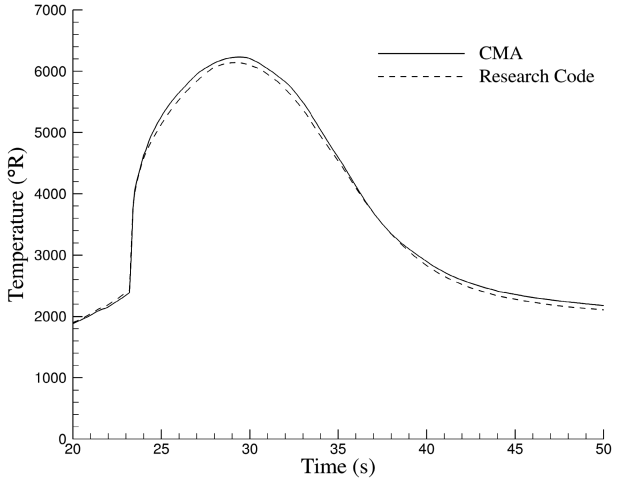

Fig. 9 Comparison of surface temperature predictions for the carbon–phenolic thermochemical ablation verification problem.

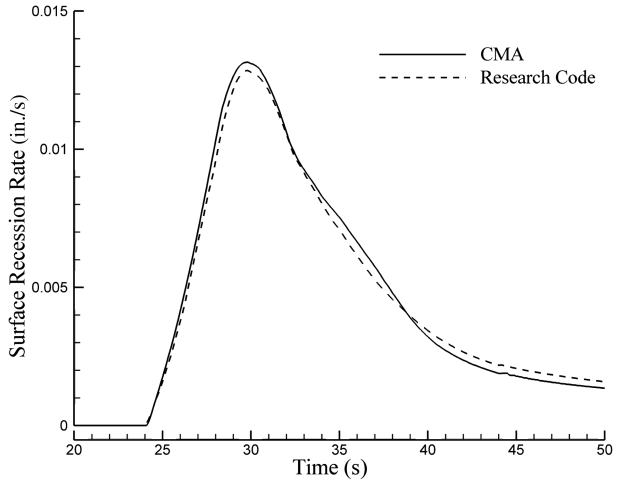

Fig. 10 Comparison of surface recession rate predictions for the carbon–phenolic thermochemical ablation verification problem.

heat capacity and thermal conductivity for gases are generally much lower than they are for a solid.

E. Porous Flow Results

One of the primary goals of this study is the implementation and verification of the gas phase continuity equation with porous flow assumptions to predict in-depth pressure in a charring ablator. Figures 11–15 show profile histories for several properties in the charring carbon–phenolic ablator, including pressure, which is predicted by solving the gas phase continuity equation with porous flow assumptions. It is evident that the solid density, pressure, and solid decomposition (or gas generation) rate profiles have steep gradients when compared with the temperature profile. This suggests that if a submesh scheme is implemented, as was done by Moyer and Rindal [1], then both the solid and gas phase continuity equations should be solved on the submesh.

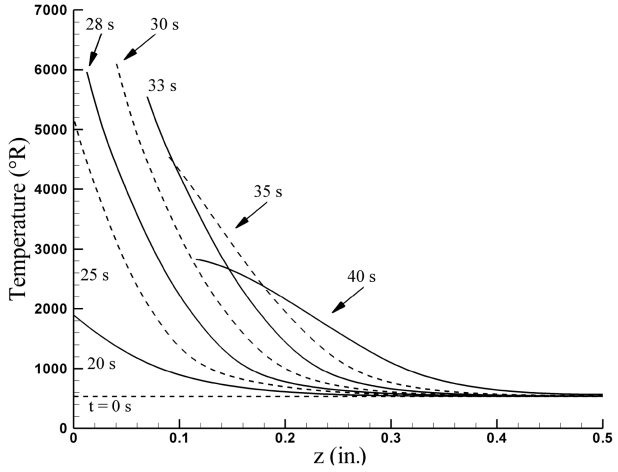

Fig. 11 Temperature profile history for the carbon–phenolic thermochemical ablation verification problem.

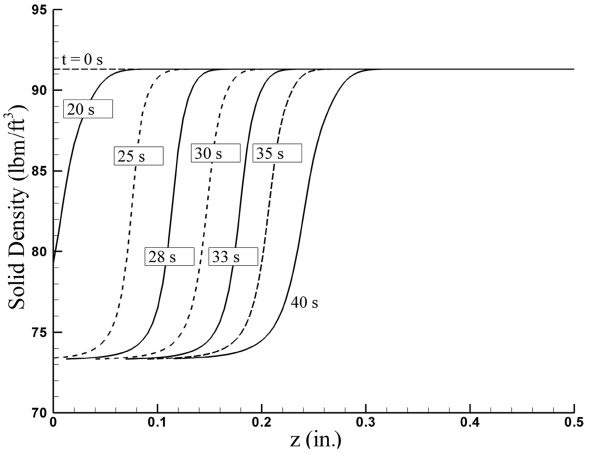

Fig. 12 Solid density profile history for the carbon–phenolic thermochemical ablation verification problem.

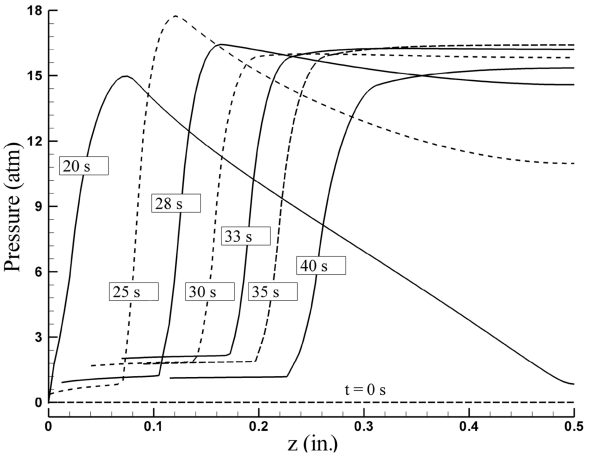

Fig. 13 Pressure profile history for the carbon–phenolic thermochemical ablation verification problem.

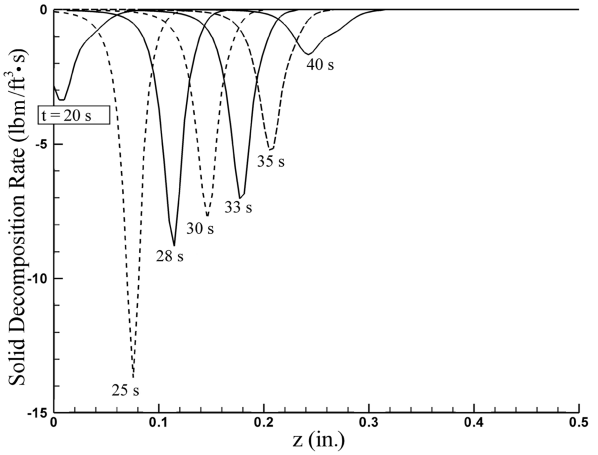

Fig. 14 Solid decomposition rate profile history for the carbon–phenolic thermochemical ablation verification problem.

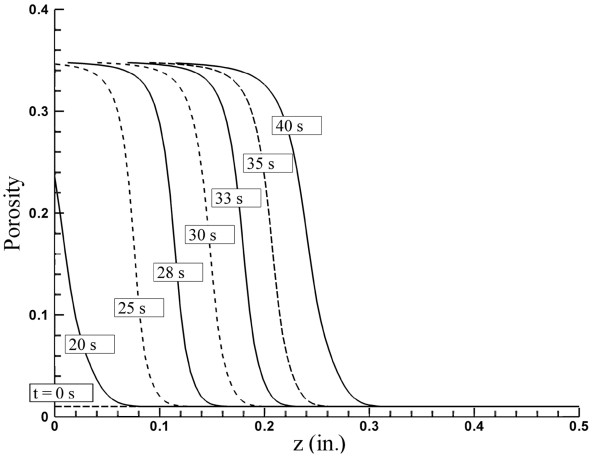

Fig. 15 Porosity profile history for the carbon-phenolic thermochemical ablation verification problem.

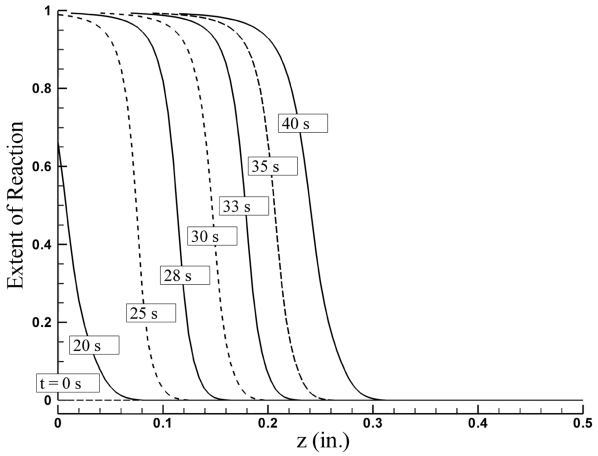

Fig. 16 "Extent of reaction" profile history for the carbon–phenolic thermochemical ablation verification problem.

It should be noted that the gas density field was initialized with a trace amount of pyrolysis gas in the pore space to avoid numerical problems once the gas continuity equation begins to be solved. A study was performed to see the solution's sensitivity to this initialization value, and it was found that the solution was nearly unaffected as long as the value was a few orders of magnitude smaller than the gas density levels present once decomposition begins.

The initial condition that would best represent reality is difficult to determine because it depends on a vehicle's ascent and time spent in low-pressure conditions outside of the Earth's atmosphere. However, because the pore space was initialized to near-vacuum conditions, the initial pyrolysis sends gas both toward the surface and to the impermeable back face where a pressure rise is evident, as seen in Fig. 13.

Figure 16 shows that ablation begins to occur before the surface solid becomes fully charred, meaning that there is still nondecomposed resin in the solid. This creates a discrepancy because the surface thermochemical solution assumes that the solid participating in the reactions is fully charred. According to the decomposition kinetics, it takes an infinite amount of time for the composite to decompose to its char state. As a result, to ensure that the thermochemistry data is accurately describing the surface ablation phenomenon, a tolerance in the vicinity of the char density could be implemented with which the solid density is automatically adjusted to the char value once this tolerance has been reached. This method is implemented in CMA, but it adds the additional complication of accounting for this mass when solving the gas phase continuity equation.

IX. Conclusions

A one-dimensional charring ablator thermal response code with pyrolysis gas flow has been developed and verified to exhibit second-order spatial accuracy for the thermochemical ablation of a decomposing material. Newton's method for the entire system of equations has been implemented and has also been verified to exhibit second-order nonlinear convergence rates for both the mixture energy and gas phase continuity equations. In addition, the block Gauss–Seidel method has been shown to converge linearly for the global system of equations. The model has shown good agreement with CMA, but it also includes several improvements in the solution procedure, which include the calculation of time-accurate nonlinearities, the improved integration of decomposition kinetics, and the prediction of pyrolysis gas flow and pore pressure.

The model presented in this study can be improved by adding more complicated physical models that could more accurately predict the thermal response of some ablators. This could include the implementation of a surface thermochemical model that would allow for finite rate reactions instead of assuming thermochemical equilibrium at the surface, as was done in this study. The assumption of in-depth thermal equilibrium between the solid and pyrolysis gas could also be eliminated by the addition of a second energy equation. There are also other material-specific models that could be included. For example, some materials exhibit coking phenomena, which is when the pyrolysis gases deposit residue in the char layer and change the density and chemical profile. Also, silica-based materials are known to form melted glass that could flow along the surface at certain conditions. However, the addition of such models could still be verified with the procedure outlined in this paper.

It should again be emphasized that verification is a necessary step in any code development process. It aids in the identification of both derivation and coding bugs that could affect the accuracy and performance of a code. Although the model presented in this code does not account for all the physics of every ablative material, the solution technique and verification process can be extended beyond the scope of the equation set presented here.

Acknowledgments

The authors would like to thank Dave Kuntz and Don Potter for their involvement in technical discussions. In addition, A. J. Amar would like to thank Basil Hassan for his support throughout the project. Sandia is a multiprogram laboratory operated by Sandia Corporation, a Lockheed Martin Company, for the U.S. Department of Energy's National Nuclear Security Administration under contract DE-AC04-94AL85000.

References

[1] Moyer, C. B., and Rindal, R. A., "An Analysis of the Coupled Chemically Reacting Boundary Layer and Charring Ablator, Part II, Finite Difference Solution for the In-Depth Response of Charring Materials Considering Surface Chemical and Energy Balances," NASA CR-1061, June 1968.

[2] Suzuki, T., Sawada, K., Yamada, T., and Inatani, Y., "Thermal Response of Ablative Test Piece in Arc-Heated Wind Tunnel," AIAA Paper 2004-341, Jan. 2004.

[3] Blackwell, B. F., "Numerical Prediction of One-Dimensional Ablation Using a Finite Control Volume Procedure with Exponential Differencing," *Numerical Heat Transfer*, Vol. 14, No. 1, 1988, pp. 17–34. doi:10.1080/10407788808913631

[4] Blackwell, B. F., and Hogan, R. E., "One-Dimensional Ablation Using Landau Transformation and Finite Control Volume Procedure," *Journal of Thermophysics and Heat Transfer*, Vol. 8, No. 2, 1994, pp. 282–287. doi:10.2514/3.535

[5] Hogan, R. E., Blackwell, B. F., and Cochran, R. J., "Application of Moving Grid Control Volume Finite Element Method to Ablation Problems," *Journal of Thermophysics and Heat Transfer*, Vol. 10, No. 2, 1996, pp. 312–319. doi:10.2514/3.789

[6] Suzuki, T., Sawada, K., Yamada, T., and Inatani, Y., "Experimental and Numerical Study of Pyrolysis Gas Pressure in Ablating Test Piece," *Journal of Thermophysics and Heat Transfer*, Vol. 19, No. 3, 2005, pp. 266–272. doi:10.2514/1.12211

[7] Suzuki, T., Sakai, T., and Yamada, T., "Calculation of Thermal Response of Ablator Under Arcjet Flow Condition," *Journal of Thermophysics and Heat Transfer*, Vol. 21, No. 2, 2007, pp. 257–266. doi:10.2514/1.25499

[8] Chen, Y.-K., and Milos, F. S., "Ablation and Thermal Response Program for Spacecraft Heatshield Analysis," *Journal of Spacecraft and Rockets*, Vol. 36, No. 3, 1999, pp. 475–583. doi:10.2514/2.3469

[9] Chen, Y.-K., and Milos, F. S., "Two-Dimensional Implicit Thermal Response and Ablation Program for Charring Materials on Hypersonic Space Vehicles," AIAA Paper 2000-0206, Jan. 2000.

[10] Chen, Y.-K., and Milos, F. S., "Three-Dimensional Ablation and Thermal Response Simulation System," AIAA Paper 2005-5064, June 2005.

[11] Milos, F. S., and Chen, Y.-K., "Two-Dimensional Ablation, Thermal Response, and Sizing Program for Pyrolyzing Ablators," AIAA Paper 2008-1223, Jan. 2008.

[12] Chen, Y.-K., Milos, F. S., and Gokcen, T., "Loosely Coupled Simulation for Two-Dimensional Ablation and Shape Change," AIAA Paper 2008-3802, June 2008.

[13] Amar, A. J., Blackwell, B. F., and Edwards, J. R., "One-Dimensional Ablation Using a Full Newton's Method and Finite Control Volume Procedure," *Journal of Thermophysics and Heat Transfer*, Vol. 22, No. 1, 2008, pp. 71–82. doi:10.2514/1.29610

[14] Roache, P. J., *Verification and Validation in Computational Science and Engineering*, Hermosa Publishers, Albuquerque, NM, 1998.

[15] Amar, A. J., "Modeling of One-Dimensional Ablation with Porous Flow Using Finite Control Volume Procedure," Masters Thesis, North Carolina State Univ., Raleigh, NC, 2006.

[16] Darcy, H., *Les Fontaines Publiques de la Ville Dijon*, Dalmont, Paris, 1856.

[17] Martin, A., and Boyd, I. D., "Simulation of Pyrolysis Gas Within a Thermal Protection System," AIAA Paper 2008-3805, June, 2008.

[18] Goldstein, H. E., "Kinetics of Nylon and Phenolic Pyrolysis," Lockheed Missiles and Space Company, Rept. AD0667181, Sunnyvale, CA, 1965.

[19] Keyhani, M., and Krishnan, V., "A One-Dimensional Model for the Thermal Response of a Decomposing Polymer," *Computational Mechanics of Porous Materials and Their Thermal Decomposition*, AMD-Vol. 136, American Society of Mechanical Engineers, Fairfield, NJ, 1992, pp. 81–90.